Journal of Magnetic Resonance **138,** 256–267 (1999)
Article ID jmre.1999.1740, available online at http://www.idealibrary.com on IDEAL®

Fluorine-19 Solid-State NMR Magic-Angle-Turning Experiments Using Multiple-Pulse Homonuclear Decoupling

Eric Hughes, Eric B. Brouwer, and Robin K. Harris[1]

Department of Chemistry, South Road Laboratories, University of Durham, Durham DH1 3LE, United Kingdom

Received November 2, 1998; February 23, 1999

For compounds giving "crowded" 1-dimensional magic-angle-spinning spectra, information about the local atomic environment in the form of the chemical shift anisotropy (CSA) is sacrificed for high resolution of the less informative isotropic chemical shift. Magic-angle-turning (MAT) NMR pulse sequences preserve the CSA information by correlating it to the isotropic chemical shift in a 2-dimensional experiment. For low natural abundance nuclei such as ^{13}C and ^{15}N and under ^{1}H heteronuclear dipolar decoupling conditions, the dominant NMR interaction is the chemical shift. For abundant nuclei such as ^{1}H, ^{19}F, and ^{31}P, the homonuclear dipolar interaction becomes a significant contribution to the observed linewidth in both F_1 and F_2 dimensions. We incorporate MREV8 homonuclear multiple-pulse decoupling sequences into the MAT experiment to give a multiple-pulse MAT (MP-MAT) experiment in which the homonuclear dipolar interaction is suppressed while maintaining the chemical shift information. Extensive use of computer simulation using GAMMA has guided the pulse sequence development. In particular, we show how the MREV8 pulses can be incorporated into a quadrature-detected sequence such as MAT. The MP-MAT technique is demonstrated for a model two-site system containing a mixture of silver trifluoroacetate and calcium difluoride. The resolution in the isotropic evolution dimension is improved by faster sample spinning, shorter MREV8 cycle times in the evolution dimension, and modifications of the MAT component of the pulse sequence. © 1999 Academic Press

Key Words: **fluorine-19; magic-angle turning; homonuclear decoupling; solid state; pulse sequence.**

INTRODUCTION

Valuable electronic, structural, and dynamic information about molecules in the solid state is obtained from the NMR chemical shift anisotropy (CSA). For powdered solids, the CSA is characterized experimentally by powder patterns for stationary samples or by the amplitude and frequency of the spinning sideband manifolds obtained under magic-angle-spinning (MAS) conditions. While CSA determinations are relatively straightforward for samples containing isolated equivalent nuclei, powder pattern and spinning sideband manifold overlap complicates similar CSA measurements for multiple-site systems. To address this problem of spectral overlap, 2-dimensional NMR techniques have been developed to correlate the CSA to the isotropic chemical shift (*1*). Two strategies have been employed (*2*): the first correlates the isotropic chemical shift acquired under MAS conditions to the CSA collected in the t_b evolution dimension, while the second correlates the CSA t_a acquisition dimension to the isotropic chemical shift developed during the t_b evolution dimension. Into this latter category falls the magic-angle-turning (MAT) experiment.

In MAT and the related magic-angle-hopping (MAH) (*3*) experiments, the sample is moved in three, equally spaced successive steps about the magic angle so that static (MAH) or pseudo-static CSA (MAT) spectra are collected in the t_a acquisition dimension (Fig. 1). Each evolution increment Δt_b is divided into three time segments $\Delta t_b/3$, separated in sample orientation by 120°, which averages the principal components of the chemical shift to the isotropic value. The difference between the two experiments lies in how this sample movement is effected: the MAH variant employs discrete "hops" whereas the MAT experiment employs very slow continuous turning (ν_{rot} = 30–600 Hz) of the sample. For the MAT experiment, the start of each evolution increment $\Delta t_b/3$ is rotor-synchronized and begins at times 0, $1/3\tau_{rot}$, and $2/3\tau_{rot}$ where $\tau_{rot} = 1/\nu_{rot}$ = the rotor period.

MAT experiments incorporating high-power ^{1}H decoupling and ^{1}H cross-polarization techniques have been applied successfully to dilute spin-1/2 nuclei such as ^{13}C and ^{15}N (*4–12*). CSA values in solid organic samples containing up to 15 different ^{13}C nuclei have been resolved (*10*). However, current MAT techniques cannot be applied directly to samples containing abundant spin-1/2 nuclei such as ^{1}H, ^{19}F, and ^{31}P since the large homonuclear dipolar interaction present in such systems obscures the chemical shift information. The inability to measure the chemical shift in the presence of such homonuclear dipolar interactions hinders the determination of ^{1}H, ^{19}F, and ^{31}P CSA values in systems for which there may already be limited structural, electronic, and dynamic information. Materials for which diffraction techniques in particular are limited and which would thus benefit from CSA characterization include fluorine- and proton-containing polymers (*2, 13*), inorganic glasses (*14*), mesoporous materials (*15*), and

[1] To whom correspondence should be addressed. Fax: +0044 191 386 1127. E-mail: r.k.harris@dur.ac.uk.

1090-7807/99 $30.00

phosphorus-containing bioorganic solids (*16*). Furthermore, we note that the electronic features of hydrogen-bonded systems are accessible from the ^{1}H CSA values (*17, 18*).

In this paper, we present the incorporation of multiple-pulse (MP) homonuclear dipolar decoupling into MAT NMR sequences to effect the removal of the homonuclear dipolar interaction in order to obtain high-resolution chemical shift and CSA correlation spectra. The strategy of combining the MREV8 multiple-pulse sequence into a MAT experiment is developed and then demonstrated for one- and two-site ^{19}F-containing samples. We show that a direct combination of the MREV8 and MAT sequences is not possible, but can be successfully implemented with appropriate modification of the MREV8 sequence. Finally, strategies to enhance the resolution in the isotropic evolution t_b-dimension are presented and evaluated.

EXPERIMENTAL

Microcrystalline solids of silver trifluoroacetate (AgO_2CCF_3, Aldrich) and calcium difluoride (CaF_2, Aldrich) were used without any additional purification.

The NMR spectra were collected on a Chemagnetics CMX200 spectrometer operating at 200.13 MHz for protons and 188.29 MHz for fluorine. A commercially available Chemagnetics H–F double-resonance APEX spinning probe was used with 4-mm (od) pencil zirconia rotors, together with fluorine-free Vespel drive tips and spacer inserts. In order to minimize both the $\mathbf{B}_0$ and $\mathbf{B}_1$ field inhomogeneities the sample was confined to the central 2 mm of the rotor. The probe magic angle was set by minimizing the ^{19}F linewidth of *p*-tert-butylcalix[4]arene-α,α,α-trifluorotoluene (*19*).

For the turning experiments requiring low spinning rates (ν_{rot} = 30–600 Hz), a special drive tip without flutes was used in conjunction with a special brass constrictor tube (0.8 mm (id), 26 mm long) placed in the line carrying the drive air. Sample spinning was controlled by manual adjustment of the drive and bearing air pressures for frequencies $\nu_{rot} < 300$ Hz and automatically for spinning frequencies >300 Hz. Air pressures for the bearing and drive of 10 and 2 psi, respectively, give a spinning rate of ~50 Hz which remains constant (±1 Hz) over the course of the experiments (up to 12 h). In contrast to other MAT-type experiments, the sample spinning is not placed under an electronic feedback control system (*5*). A Bruker CXP amplifier operating in class C mode was used for ^{19}F RF irradiation. All experiments were carried out at ambient temperatures.

The standard multiple pulse probe tune-up for ^{19}F was followed (*20*). The 45, 90, 135, 180, 225, 270, and 310° pulses were set using a sample of C_6F_6 held in a glass sphere and placed at the center of the probe coil. The 1-D MREV8 spectra were collected using the quadrature-detected pulse sequence of Barbara and Baltusis (*21*). MREV8 acquisition cycle times of t_c = 36 to 40.8 μs were used (corresponding to τ values of 3.0 to 3.4 μs), with 90° pulse durations of 1.36 to 1.45 μs. An integral multiple of the MREV8 acquisition cycle was used for the evolution dwell time in order to minimize the spectral width in the t_1 dimension. The scaling of the chemical shift in the evolution dimension was calibrated using a sample of silver trifluoroacetate (AgTFA) by collection of data with the transmitter offset at 1-kHz increments from the isotropic peak at 188.2965514 MHz. Further NMR experimental details are given in the appropriate figure captions. T_1 measurements were carried out under MREV8 conditions using the saturation-recovery method: AgTFA (1.2 s) and calcium difluoride (>20 s).

The computer simulations were carried out using GAMMA version 3.5β (*22*) on a Sun ultrasparc1 workstation. Simulation of a two-site, 2-D MP-MAT spectrum took approximately 12 h. The simulated data were output in the Chemagnetics Spinsight data format and are processed in the same way as experimental data.

RESULTS AND DISCUSSION

(a) The Magic-Angle-Hopping and -Turning Experiments

The theory for MAH and MAT has been described in detail in previous publications (*1, 3, 5*). For now, we will consider a brief overview of the theory and features of both experiments relevant to the incorporation of multiple-pulse sequences. In particular, the MAH sequence is examined and developed in the context of the GAMMA simulation work. The relevant features of the MAH sequence are then brought to bear on the subsequent development of the MAT experiments.

The generalized MAT pulse sequence is depicted in Fig. 1. The pulses are synchronized to the rotor orientation as it rotates about the magic angle. The first segment starts at time $\tau_{rot} = 0$, at which point the magnetization evolves for time $t_b/3$ through an angle Φ_1 in the *xy* plane. Selection of either the cosine or the sine component by a projection pulse p_1 stores the magnetization along the longitudinal axis for the duration, *L*, of this time segment. The remaining transverse component is purged by T_2 relaxation and dispersion (note that $T_1 \gg T_2$). After a time of $\tau_{rot}/3$, the sample has rotated by 120°, and a tipping pulse r_2 allows the magnetization to evolve in the *xy* plane for time $t_b/3$ through an angle Φ_2; one of the transverse components is selected (p_2) in a similar manner. This is repeated for the final time period, at which point the FID is acquired. Since the magnetization has evolved under the chemical shift interaction in three mutually perpendicular directions (when viewed from the sample), the summed signal gives the isotropic chemical shift according to

$$\omega_x + \omega_y + \omega_z = 3\omega_{iso}. \quad [1]$$

In a collection of a 2-dimensional hypercomplex data set, Eq. [1] holds true for specific values of the projection pulse phases p_i and appropriate combinations of the respective FIDs. A

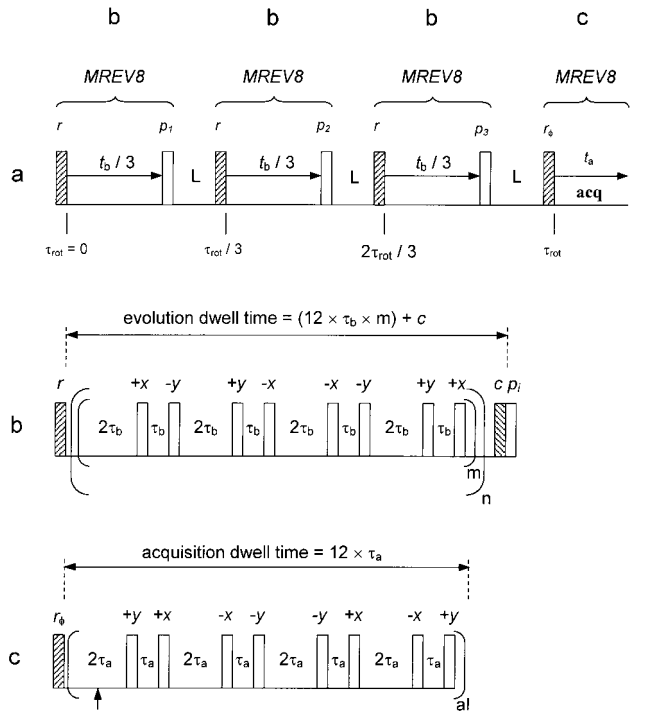

FIG. 1. Pulse sequence for the 2-dimensional magic-angle-turning (MAT) NMR experiment: (a) basic MAT pulse sequence (*1*) which becomes the multiple-pulse MAT (MP-MAT) sequence upon addition of MREV8 homonuclear decoupling during the (b) evolution and (c) acquisition dimensions. All pulses are 90° except for *c* (45°) and r_ϕ (see text); L refers to the magnetization storage period, r_i are the read pulses, and p_i are the projection pulses. In (b) the number of MREV8 cycles per evolution dwell time increment, Δt_a, is m, while n is the number of evolution increments. In (c) the arrow indicates the sampling window and al is the number of collected acquisition points.

2-dimensional spectrum with an isotropic chemical shift dimension is produced from a set of FIDs in which the amplitude is modulated by the functions $\cos(\Phi_1 + \Phi_2 + \Phi_3)$ and $\sin(\Phi_1 + \Phi_2 + \Phi_3)$. Eight combinations of the phases of the three projection pulses p_i:

$$F_1(t_b, t_a) = \cos(\Phi_1) \times \cos(\Phi_2) \times \cos(\Phi_3) F_a(t_a) \quad [2]$$

$$F_2(t_b, t_a) = -\sin(\Phi_1) \times \sin(\Phi_2) \times \cos(\Phi_3) F_a(t_a) \quad [3]$$

$$F_3(t_b, t_a) = -\sin(\Phi_1) \times \cos(\Phi_2) \times \sin(\Phi_3) F_a(t_a) \quad [4]$$

$$F_4(t_b, t_a) = -\cos(\Phi_1) \times \sin(\Phi_2) \times \sin(\Phi_3) F_a(t_a) \quad [5]$$

$$F_5(t_b, t_a) = \sin(\Phi_1) \times \cos(\Phi_2) \times \cos(\Phi_3) F_a(t_a) \quad [6]$$

$$F_6(t_b, t_a) = \cos(\Phi_1) \times \sin(\Phi_2) \times \cos(\Phi_3) F_a(t_a) \quad [7]$$

$$F_7(t_b, t_a) = \cos(\Phi_1) \times \cos(\Phi_2) \times \sin(\Phi_3) F_a(t_a) \quad [8]$$

$$F_8(t_b, t_a) = -\sin(\Phi_1) \times \sin(\Phi_2) \times \sin(\Phi_3) F_a(t_a) \quad [9]$$

generate the required cosine- and sine-modulated FIDs:

$$F_1 + F_2 + F_3 + F_4 = \cos(\Phi_1 + \Phi_2 + \Phi_3) F_a(t_a) = F_{real} \quad [10]$$

$$F_5 + F_6 + F_7 + F_8 = \sin(\Phi_1 + \Phi_2 + \Phi_3) F_a(t_a) = F_{imag}, \quad [11]$$

where $F_a(t_a)$ is the acquired complex FID.

Table 1 collects the basic pulse phases for the prototype full MAH or MAT sequence (after Hu *et al.* (*1*)). Only the phases of the first projection pulse p_1 and the receiver differ between the two F_{real} and F_{imag} data sets. In a hypercomplex MAT experiment F_{real} and F_{imag} are collected sequentially and combined in subsequent processing to give an absorption–absorption-phased 2-dimensional spectrum.

The full MAT pulse sequence (Fig. 1a) has two disadvantages for spin-dilute nuclei (*1*, *5*): First, loss of magnetization due to three longitudinal storage periods lowers the signal-to-noise ratio. Second, acquisition begins immediately after the final read pulse r_ϕ and may be adversely influenced by probe dead-time and receiver ring-down effects. The incorporation of the third evolution period into the acquisition period both improves the signal-to-noise ratio and reduces baseplane distortions (*4*). While the signal-to-noise ratio of the full MAT sequence may be a disadvantage for low natural abundance nuclei, it is less of a disadvantage for the higher sensitivity and natural abundance of ^{1}H, ^{19}F, and ^{31}P. Furthermore, baseplane distortions are reduced since external RF filters are not required and the probes are designed to have short ring-down. We begin by incorporating a MREV8 multiple-pulse sequence into the full MAH and MAT pulse sequences described in Fig. 1 and conclude with some of the pulse sequence improvements mentioned above.

(b) GAMMA Simulation of the MAH Experiment

Theoretical considerations. The introduction of a multiple-pulse homonuclear decoupling sequence within the MAT

TABLE 1
The Basic Phase Table for the MAH and MAT Pulse Sequences in Fig. 1

	$F_{real} = F_1 + F_2 + F_3 + F_4$				$F_{imag} = F_5 + F_6 + F_7 + F_8$			
nt	1	2	3	4	5	6	7	8
r	*Y*	*Y*	*Y*	*Y*	*Y*	*Y*	*Y*	*Y*
p_1	*X*	*Y*	*Y*	*X*	*Y*	*X*	*X*	*Y*
p_2	*X*	*Y*	*X*	*Y*	*X*	*Y*	*X*	*Y*
p_3	*X*	*X*	*Y*	*Y*	*X*	*X*	*Y*	*Y*
rcvr	*X*	$\bar{X}$	$\bar{X}$	$\bar{X}$	$\bar{X}$	$\bar{X}$	$\bar{X}$	*X*
FID	F_1	F_2	F_3	F_4	F_5	F_6	F_7	F_8

Note. nt represents the transition number.

experiment has been achieved through the extensive use of computer simulations. The object-oriented GAMMA (*22*) package was used to simulate various aspects of the experiment using a density matrix approach. In the MAT experiment, the rotor in which the sample is packed is slowly rotated about the magic angle in order to spatially select the three components of the chemical shift tensor during the t_b evolution periods. Therefore, the Hamiltonian describing the system is time dependent, continuously changing as the rotor turns. To simulate such an experiment using a density matrix approach requires that the rotor period be split up into small increments, over which the Hamiltonian can be assumed constant. For each increment the Hamiltonian is recalculated and the density matrix evolved. Alternatively, a solution based on Floquet methods (*23, 24*) could be pursued to render the Hamiltonian constant over the full rotor period. However, it was felt that both methods would be too complicated and computer intensive to implement successfully. Therefore, instead of attempting to simulate the turning experiment of Gan (*4*), it was decided to investigate the possibilities of simulating the original hopping (MAH) experiment of Bax and co-workers (*3*).

The MAH experiment is essentially a static experiment, and therefore the Hamiltonian describing the system is time independent. Evolution under the three different components of the chemical shift tensor is brought about by a rapid rotation of the sample by 120° about the magic angle at the end of the evolution period. In a simulation, therefore, a constant Hamiltonian can be used to propagate the density matrix during each third of the MAH experiment. This reduces the complexity of the simulation and also decreases the execution time. The main purpose of attempting to simulate the MAH experiment is to guide the incorporation of a multiple-pulse sequence into the evolution and detection periods of the MAT experiment. At this stage the effectiveness of the multiple-pulse sequence to remove the homonuclear dipolar interaction is not under investigation, and therefore a system consisting of isolated equivalent spins was used. The system then evolves under a chemical shift Hamiltonian alone. However, we have used two mutually isolated spin baths, each consisting of an ensemble of equivalent ^{19}F nuclei (ignoring both dipolar and indirect coupling) as the basis of the 2-D simulations calculated in this paper to show more clearly how the phase cycling of the final pulse sequence behaves. This case will be referred to as a two-spin system.

In the computer simulation, the total Hamiltonian, H_{TOT} for the two-spin system is

$$H_{TOT} = H_Z + H_{cs}^1 + H_{cs}^2, \qquad [12]$$

where H_Z is the Zeeman Hamiltonian and H_{cs}^1 and H_{cs}^2 are the chemical shift Hamiltonians for the two spin types. In order to arrive at the final expressions for the Hamiltonian used in the simulation (which incorporates the spatial dependence of the motion of the sample about the magic angle), we have used standard spherical tensor methods. We follow closely the work of Haeberlen (*25*) and Maricq and Waugh (*26*).

The individual terms of the Hamiltonian can be expressed as the product of second-rank tensors by the equation

$$H^\lambda = C^\lambda \sum_l \sum_{l=-m}^{l} (-1)^m R^\lambda_{l,-m} T^\lambda_{l,m}, \qquad [13]$$

where C^λ comprises physical constants appropriate to the type of interaction λ, $R_{l,-m}$ is the spatial spherical tensor, and $T_{l,m}$ is the spin spherical tensor. The Zeeman Hamiltonian may be removed from the equation by transforming the spin tensor T into a coordinate system rotating at the Larmor frequency about the z axis in the laboratory frame. The periodic time dependence may be removed by average Hamiltonian theory (*27*), and to lowest order the Hamiltonian for a chemical shift interaction is

$$H_0^{CS} = C^{CS} \sum_{i=1}^{2} (R_{00}^{CS} T_{00}^{CS} + R_{20}^{CS} T_{20}^{CS})_i, \qquad [14]$$

where i is nuclear spin index. Both the spin and the spatial tensors are expressed in the laboratory frame. The spatial tensor is diagonal in its principal axis system (PAS) and can be related back to the laboratory frame by applying two successive rotational transformations so that the tensor goes through an intermediate reference frame fixed in the sample rotor. The R_{00} component represents the isotropic chemical shift and is invariant under rotation. The R_{20} components may be rotated using standard Wigner rotation matrices in the equation

$$R^{\lambda,i}_{l,m} = \sum_{m'} D^l_{m',m}(\alpha^\lambda, \beta^\lambda, \gamma^\lambda) \rho^{\lambda,i}_{l,m'}, \qquad [15]$$

where l is the rank of the tensor, α, β, and γ are the Euler angles, and $\rho_{l,m}$ the components of the irreducible spherical tensor in the new reference frame. The definition of the Euler angle matrix elements is given by Spiess (*28*). With two rotations, for R_{20} this is then

$$R^{CS,i}_{2,0} = \sum_{m'=-2}^{2} D^2_{m',0}(0, \theta, \omega_r t) \sum_{m''=-2}^{2} D^2_{m'',m'}(\alpha, \beta, \gamma) \rho^{CS,i}_{2,m''}, \qquad [16]$$

where the $\rho_{2\pm1}$ are zero for the chemical shift interaction. The angles α, β and γ relate the principal axis system of the chemical shift tensor to the axis system fixed in the rotor spinner. The angles θ and $\omega_r t$ relate the rotor-fixed axis system to the laboratory axis system. In the simulations, we restrict ourselves to an axially symmetric tensor, which allows the $\rho_{2\pm2}$

terms to be set to zero to reduce computational time. Thus, the only terms required in the simulations arise from ρ_{20}. Substitution of the correct Wigner matrix elements gives

$$R_{2,0}^{\mathrm{CS},i} = \left(\frac{3\cos^2\theta - 1}{2}\right)\left(\frac{3\cos^2\beta - 1}{2}\right)\rho_{2,0}^{\mathrm{CS},i} + \tfrac{3}{4}\sin^2\theta\sin^2\beta\cos(2\omega_r t + 2\gamma)\rho_{2,0}^{\mathrm{CS},i} - \tfrac{3}{4}\sin 2\theta\sin 2\beta\cos(\omega_r t + \gamma)\rho_{2,0}^{\mathrm{CS},i}. \quad [17]$$

In the principal axis system of the chemical shift tensor $\rho_{2,0}^{\mathrm{CS}} = \sqrt{3/2}\zeta$ and $\rho_{0,0}^{\mathrm{CS}} = \delta_{\mathrm{iso}}$, where δ_{iso} is the isotropic chemical shift and $3\zeta/2 = \delta_{33} - \frac{1}{2}(\delta_{11} + \delta_{22})$ the chemical shift anisotropy. For the spin tensor $T_{00}^{\mathrm{CS},i} = I_0^i B_0$ and $T_{00}^{\mathrm{CS},i} = \sqrt{2/3} I_0^i B_0$. On substitution into Eq. [14] one gets, in angular frequency units

$$H_0 = \sum_i \left(\gamma_i \delta_{\mathrm{iso}}^i I_0 B_0 + \gamma_i \xi^i \left[\left(\frac{3\cos^2\theta - 1}{2}\right)\left(\frac{3\cos^2\beta - 1}{2}\right) + \tfrac{3}{4}\sin^2\theta\sin^2\beta\cos(2\omega_r t + 2\gamma) - \tfrac{3}{4}\sin 2\theta\sin 2\beta\cos(\omega_r t + \gamma)\right] I_0^i B_0\right). \quad [18]$$

When $\theta = 54.7°$ (the magic angle) and with $\omega_0 = \gamma_0 B_0$, Eq. [18] simplifies to

$$H_0 = \sum_i \omega_0^i(\delta_{\mathrm{iso}}^i + \zeta^i[\tfrac{3}{4}\sin^2\theta\sin^2\beta\cos(2\omega_r t + 2\gamma) - \tfrac{3}{4}\sin 2\theta\sin 2\beta\cos(\omega_r t + \gamma)])I_0^i. \quad [19]$$

Since the MAH experiments evolve under a time-independent Hamiltonian during the acquisition period, Eq. [19] can be simplified further, so that it is dependent only on one angle. This reduction is achieved by taking the PAS frame directly into the laboratory frame and bypassing the axis system fixed in the rotor. Equation [19] then becomes

$$H_0 = \sum_i \omega_0^i\left(\delta_{\mathrm{iso}}^i + \zeta^i\left(\frac{3\cos^2\beta - 1}{2}\right)\right) I_0^i. \quad [20]$$

This simplification reduces the number of points required for an adequate powder average considerably. In the t_b dimension the powder average is performed over the two angles γ and β. The crystallite orientations in the powder average were calculated using Hammersley points (*29, 30*). This method is comparable to those of Conroy (*31*) and Wolfsberg (*32*) but has the advantage that it is not restricted to specific set sizes.

MAH with MREV8 decoupling. It has been shown that the homonuclear dipolar couplings can be removed successfully by applying multiple-pulse decoupling techniques (*33*). Therefore, in order to use the MAT technique for abundant spins, an appropriate form of multiple-pulse selective averaging during the evolution and acquisition periods of the 2-D sequence must be introduced. We chose, in the first instance, to work with the MREV8 (*34, 35*) multiple-pulse sequence.

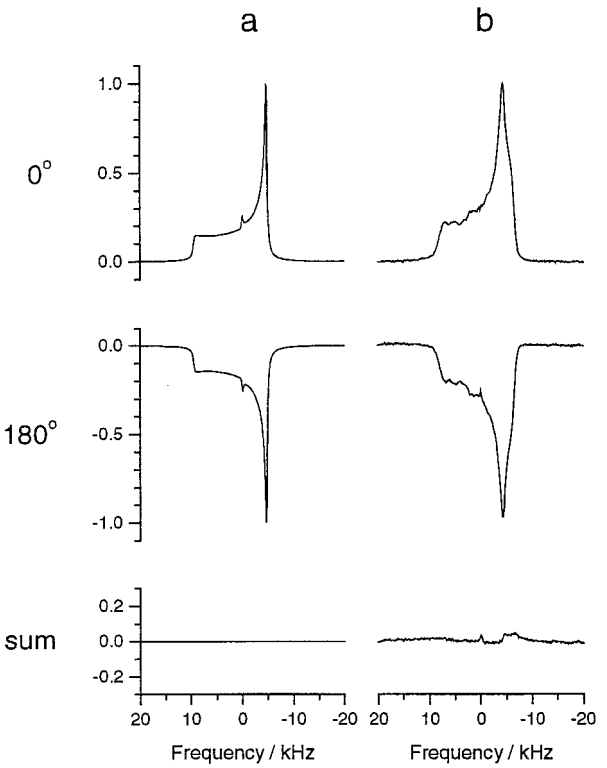

FIG. 2. ^{19}F MREV8 NMR spectrum (188.2976 MHz) of a stationary sample of AgTFA illustrating 0° (top) and 180° (middle) receiver phase selection. The bottom trace is the summed residual. (a) Simulation using an axial CSA tensor (see text). (b) Experimental: 64 acquisitions; 6-s recycle delay; 256 points collected, and zero-filled to 512; pulses: 45° = 0.81 μs, 90° = 1.36 μs, 135° = 1.91 μs, 225° = 2.99 μs, 270° = 3.53 μs, 315° = 4.26 μs.

The introduction of the MREV8 pulse sequence into both the evolution and the detection periods of the MAT experiment raises two main problems. The first involves the correct phase cycling of the receiver during the detection period in order for the MAT sequence to work properly. The second problem arises during the evolution period and is one of retaining quadrature information when the different sine and cosine components are selected after the evolution period. Under the majority of multiple-pulse decoupling sequences the effective magnetization no longer precesses about the z axis aligned along the $\mathbf{B}_0$ field, and therefore the sine and cosine components of the magnetization detected by the receiver in quadrature are no longer of the correct magnitude with respect to each other. If this is not corrected, quadrature ghosts will appear in the final 2-D spectrum.

In a MAT experiment two hypercomplex data sets are collected which are subsequently combined to form a single 2-dimensional spectrum. Each experiment, in its most simple form, consists of a four-pulse phase cycle (Table 1). For one

TABLE 2
The Basic Phase Table for the MP-MAT Pulse Sequence in Fig. 1

	F_1				F_2				F_3				F_4			
nt	1	2	3	4	5	6	7	8	9	10	11	12	13	14	15	16
r	*Y*	*Y*	*Y*	*Y*	*Y*	*Y*	*Y*	*Y*	*Y*	*Y*	*Y*	*Y*	*Y*	*Y*	*Y*	*Y*
c	*X*	*X*	*X*	*X*	*X*	*X*	*X*	*X*	*X*	*X*	*X*	*X*	*X*	*X*	*X*	*X*
p_1	*X*	*X*	*X*	*X*	*Y*	*Y*	*Y*	*Y*	*Y*	*Y*	*Y*	*Y*	*X*	*X*	*X*	*X*
p_2	*X*	*X*	*X*	*X*	*Y*	*Y*	*Y*	*Y*	*X*	*X*	*X*	*X*	*Y*	*Y*	*Y*	*Y*
p_3	*X*	*X*	*X*	*X*	*X*	*X*	*X*	*X*	*X*	*X*	*X*	*X*	*X*	*X*	*X*	*X*
r_ϕ	135	45	90	90	315	225	270	270	315	225	270	270	315	225	270	270
	Y	$\bar{Y}$	*X*	$\bar{X}$	*Y*	$\bar{Y}$	*X*	$\bar{X}$	*Y*	$\bar{Y}$	*X*	$\bar{X}$	*Y*	$\bar{Y}$	*X*	$\bar{X}$
rcvr	*Y*	$\bar{Y}$	*X*	$\bar{X}$	*Y*	$\bar{Y}$	*X*	$\bar{X}$	*Y*	$\bar{Y}$	*X*	$\bar{X}$	*Y*	$\bar{Y}$	*X*	$\bar{X}$

	F_5				F_6				F_7				F_8			
nt	1	2	3	4	5	6	7	8	9	10	11	12	13	14	15	16
p_1	*Y*	*Y*	*Y*	*Y*	*X*	*X*	*X*	*X*	*X*	*X*	*X*	*X*	*Y*	*Y*	*Y*	*Y*
r_ϕ	315	225	270	270	315	225	270	270	315	225	270	270	135	45	90	90

Note. The real (top) and imaginary (bottom) data sets are collected with variation of the phase of the projection pulse p_1 and the pulse durations (in degrees) of the final read pulse r_ϕ; *nt* represents the transition number.

experiment, during the first acquisition the receiver is set to 0° (*X*), and for the next three acquisitions it is set to 180° ($\bar{X}$). In the second experiment, the first three acquisitions have the receiver set to 180° and in the final acquisition the receiver is set to 0°. With the addition of the MREV8 sequence during the acquisition stage, one can no longer simply change the receiver phase to achieve the correct 180° phase cycling since the precession of the magnetization is no longer along $\mathbf{B}_0$. In order to achieve the required phase cycling during acquisition, the final MAT read pulse r_ϕ must be replaced with a MREV8 sequence that preserves quadrature and can produce the necessary phase inversion of the signal.

Recently, various groups have introduced multiple-pulse sequences that preserve quadrature (*21, 36, 37*). The MREV8 sequence introduced by Barbara and Baltusis (*21*) achieves a quadrature-detected spectrum by altering the magnitude and phase of the preparation pulses so that the magnetization precesses about different axes. When the resulting FIDs are coadded, they produce a FID which has equal magnitude signals in both real and imaginary channels. The published preparation pulse durations are 45°_{270}, 135°_{90}, 90°_{0}, and 90°_{180}, where the subscript denotes both the pulse and receiver phase. We show that if each preparation pulse duration is increased by 180° so that the preparation pulses are now 225°_{270}, 315°_{90}, 270°_{0}, and 270°_{180}, then an inverted spectrum is achieved on Fourier transformation. Figure 2a shows two 1-dimensional simulated MREV8 spectra, where the lower spectrum has been inverted with respect to the top spectrum by applying the second set of preparation pulses. Figure 2b shows the results of an actual implementation of the pulse sequence using a sample of AgTFA. The summation spectrum is given at the bottom of the figure, and it is clear that the relative phases of the two spectra are very close to 180°. The inverted spectrum of the AgTFA shows a small zero-frequency spike at the transmitter, which may arise from the lower precision of the longer pulses used in the second MREV8 sequence.

More complex MAT sequences such as the MAT± (*6*) sequence (discussed later), require receiver phase cycling in steps of 90°. We have been unable to find preparation pulse duration and phase combinations that would allow the MREV8 multiple-pulse sequence to mimic such receiver phase shifts. Therefore we have followed an alternate approach to meet the receiver phase inversion requirements of the initial MAT sequence which can also be used in more complex MAT experiments. The technique involves collecting and storing separately each individual FID that makes up the phase cycle. Each FID is collected with the same receiver phase. At the end of the experiment, the appropriate phase transformation is applied to the FIDs and then they are combined to give the real and imaginary data sets. This procedure replaces what a quadrature receiver in spectrometers does automatically during data acquisition. While the above approach generates a number of temporary files, it does allow the consistent use of the shorter preparation pulses, which in turn eliminates any residual summation signal (Fig. 2) due to the lower precision in the longer preparation pulses. The final result is a better addition of the MAT acquisition FIDs and an improved 2-D spectrum.

In each of the three evolution periods of the full MAT experiment, the MREV8 sequence is required to remove the homonuclear decoupling. At the start of each period the magnetization is rotated into the *xy* plane by a single 90° read pulse *r* along the *y* axis (see Fig. 1 and Table 2). At the end of each evolution period the sine or cosine projection of the magnetization is selected and stored along the [001] *z* axis by applying

a 90° pulse p_i of the correct phase. This sequence again requires that the magnetization precess about the z axis so that the magnitude of each projection is correct. However, the MREV8 sequence upsets this situation, since magnetization precesses about the [101] rather than the [001] axis, as discussed above. In order to retain the correct quadrature relationship, a compensation pulse c is applied at the end of the MREV8 evolution period to rotate the magnetization precession back into the xy plane (*38*). For the traditional MREV8 sequence, Jackson has shown that this can be achieved with a 45° pulse applied about the y axis (*39*). With the phase cycle of the MAT sequence, each preparation pulse is along the y axis, that is 90° out of phase from the normal MREV8 preparation pulse (*21*). Therefore, all the pulses used in the MREV8 sequence during the t_b evolution periods must be increased in duration by 90°. As a result of this phase change, the effective precession axis is altered, and so the compensation pulse at the end of the evolution pulse must also be altered so that the 45° pulse is applied along the x axis. Figure 3 shows the effective precession axes for the two MREV8 sequences together with the corresponding compensation pulse that needs to be applied.

Using Eqs. [19] and [20], various aspects of the MAH experiment were simulated to see if the approach taken for the phase cycling would work. To begin with, a simple MAH experiment was simulated without any homonuclear multiple-pulse dipolar decoupling. From this basic program, two further programs were written which incorporate a homonuclear dipolar decoupling MREV8 sequence into the (a) evolution and (b) acquisition periods of the sequence. By separating this step into two programs, the effectiveness of the proposed phase cycling schemes on the evolution and acquisition periods is investigated without interference from each other. From these two simulations it was clear that the phase cycling did allow the incorporation of the MREV8 sequence into the MAH experiment. A final program combines the two earlier programs, with the MREV8 sequence in both the acquisition and evolution periods of the MAH experiment. Figure 4b shows a contour plot of a computer simulation of the final MAH experiment for the two-spin case with an MREV8 homonuclear dipolar decoupling sequence in both periods. The isotropic shifts were 1 and −2 kHz, the CSA values were 14.25 and −14.25 kHz (with both asymmetries set to 0.0), and the transmitter was set

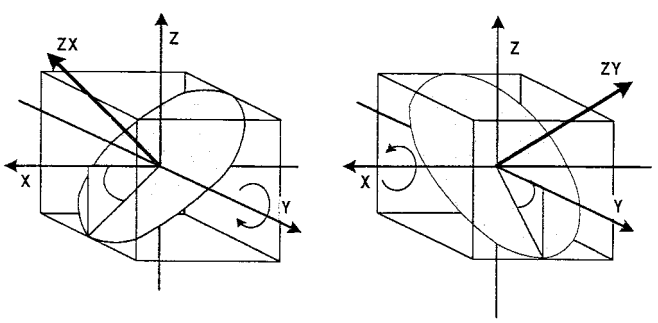

Preparation Pulse Phase	MREV8 Sequence Phases	Normalized Precession Axis	45° Quadrature Compensation Pulse
X	$(X\bar{Y})(Y\bar{X})(\bar{X}\bar{Y})(YX)$	$\frac{1}{\sqrt{2}}(1,0,1)$	Y
Y	$(YX)(\bar{X}\bar{Y})(\bar{Y}X)(\bar{X}Y)$	$\frac{1}{\sqrt{2}}(0,1,1)$	X

FIG. 3. Effective precession axes under MREV8 multiple-pulse decoupling as a function of the preparation pulse phase. Listed below are MREV8 sequence phases, the normalized precession axis, and the 45° compensation pulse c required for quadrature preservation during incorporation into the MAT sequence.

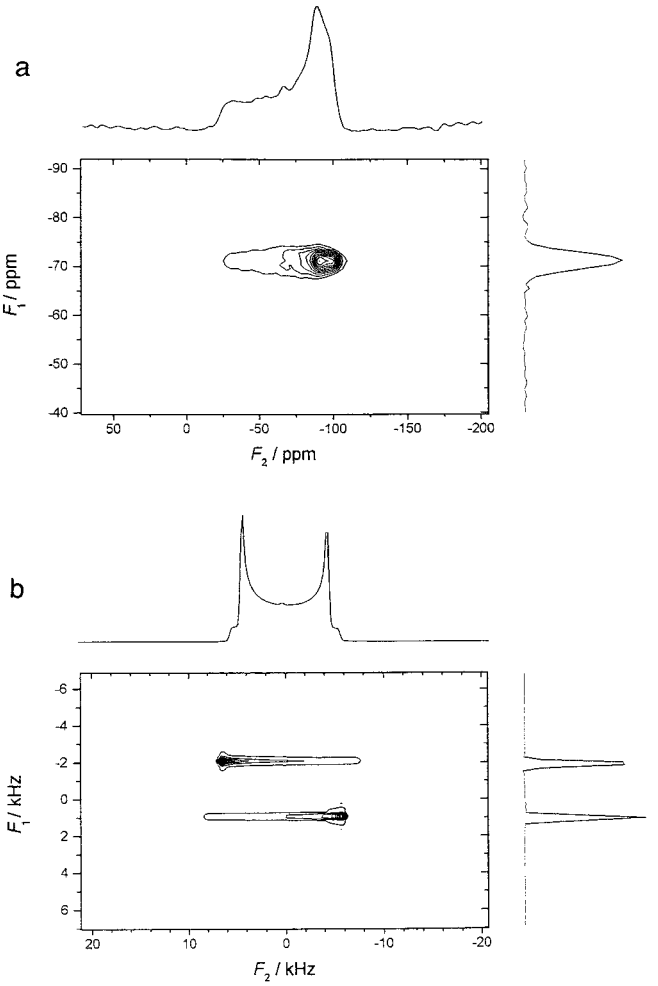

FIG. 4. ^{19}F MP-MAT NMR spectrum (188.2976 MHz) of AgTFA (a) collected at ν_{rot} = 46 Hz (τ_{rot} = 21.739 ms) using the pulse sequence of Fig. 1: 20 time increment Δt_b, 32 FIDs for each increment with a recycle delay of 6 s. The evolutionary MREV8 cycle time = 12 × 3.0 μs = 36.0 μs; each $\Delta t_b/3$ evolution increment was composed of two MREV8 sequences for a total dwell time of 2 × 3 × 36.0 μs = 216.0 μs. The total evolution time was 20 × 216.0 μs = 4320 μs. The acquisition MREV8 cycle time = Δt_a = 12 × 3.4 μs = 40.8 μs, and 256 acquisition points were collected. Total experimental time was 2.1 h. Pulses are as in Fig. 2. (b) A simulation using the MAH model as described in text. For both plots, the floor of the contour plot was set to 10% of I_{max} with 9 contours at 10% I_{max} intensity increments. Sum projections are given in both dimensions, and the chemical shift scale is corrected for MREV8 scaling of 0.499.

at 0 Hz. The MREV8 cycle time was 36 μs in both the t_a acquisition and the t_b evolution dimensions. The step increment in the evolution dimension was set equal to a single MREV8 cycle, and 64 t_b evolution increments were calculated. Relaxation of in-plane magnetization during the storage period is simulated by the setting of the off-diagonal elements of the density matrix to zero. T_2 relaxation during the acquisition and evolution periods is performed by the application of a weighting function when the data were processed. Ideal delta pulses were used in the simulation. The figure indicates that the experiment retains quadrature in both dimensions and that a pure adsorption spectrum is obtained. The small glitch at zero frequency in the anisotropic dimension arises from the variability of the precession axis of the magnetization brought about by the large chemical shift offsets (*38*).

(c) The Multiple-Pulse Magic-Angle-Turning Experiment

The ^{19}F MP-MAT NMR spectrum of AgTFA. The focus of the initial MP-MAT experiments was to examine the feasibility of the technique using AgTFA. AgTFA has a single peak in the 1-dimensional ^{19}F MAS NMR spectrum at $\delta = -71.5$ ppm and a narrow, nearly axially symmetric CSA powder pattern (*40*). Figure 4a shows the ^{19}F MP-MAT spectrum of AgTFA with sum projections along the F_2 acquisition (horizontal) and F_1 evolution (vertical) dimensions. The projections of both dimensions demonstrate the removal of the ^{19}F–^{19}F homonuclear dipolar interaction, giving 2-D spectral features arising from the chemical shift interaction alone. The pseudo-static lineshape shows a nearly axially symmetric CSA powder pattern, with values of the principal components of the chemical shift ($\delta_{11} = +45.3$ ppm, $\delta_{22} = -16.7$ ppm, $\delta_{33} = -28.7$ ppm with respect to δ_{iso}) similar to those in the literature ($\delta_{11} = +49.4$ ppm, $\delta_{22} = \delta_{33} = -24.7$ ppm) (*40*). The slight asymmetry of the current result may be a result of the higher resolution afforded by the larger magnetic field (4.7 T vs 1.35 T). The deviation from axial symmetry for a rapid rotating $-CF_3$ group may be related to molecular packing effects.

The sum projection along the F_1 isotropic evolution dimension shows that the MP-MAT experiment has removed both the homonuclear dipolar interaction and the chemical shift anisotropy. The single peak at $\delta = -71.5$ ppm has a full width at half height (FWHH) of 4.0 ppm, which is greatly reduced from the sum projection along the F_2 anisotropic acquisition dimension ($\xi = 68$ ppm). The MREV8 multiple-pulse decoupling sequence averages the homonuclear dipolar interaction to zero and partially averages the chemical shift interaction. The chemical shift, then, is scaled under MREV8 conditions by a theoretical value of $\sqrt{2}/3 = 0.471$; the actual value depends on factors such as the pulse duration, pulse imperfections, and MREV8 cycle times. The scaling factor can be determined experimentally by measuring the position of the isotropic peak as a function of the transmitter offset. Four MP-MAT experiments were carried out with the transmitter frequency set to values -1, 1, 2, and 3 kHz from the ^{19}F resonance frequency.

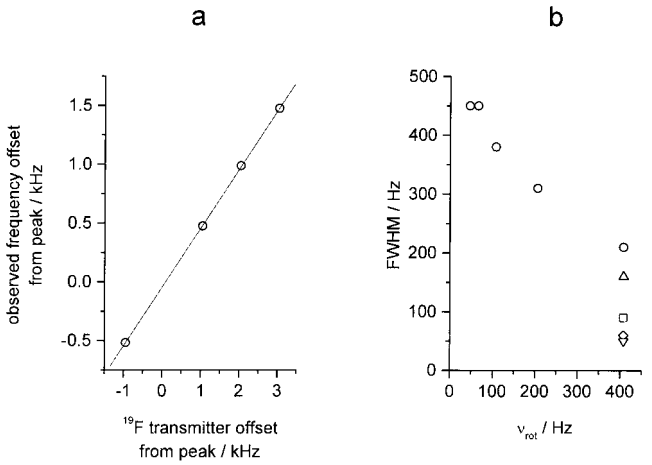

FIG. 5. (a) Determination of MREV8 scaling factor for the evolution dimension of the ^{19}F MP-MAT spectra of AgTFA. The ^{19}F transmitter was positioned -1, 1, 2, and 3 kHz from resonance, and the corresponding evolution dimension frequency offsets were measured. The slope of the fit gives a scaling factor of 0.499 $\pm$ 0.002. (b) FWHH linewidths of the ^{19}F isotropic chemical shift sum projection as a function of sample rotation frequency collected using the MP-MAT pulse sequence (○); MP-MAT$^{\pm}$, no rotational echo extensions in t_b (△); MP-MAT$^{\pm}$, one rotational echo extension in t_b (□); MP-MAT$^{\pm}$, two rotational echo extensions in t_b (◇); MP-MAT$^{\pm}$, three rotational echo extensions in t_b (▽). The MP-MAT$^{\pm}$ spectra were collected at 408 Hz ($\tau_{rot} = 2.451$ ms) using the pulse sequence depicted in Fig. 7: 188.29225 MHz, 40 time increments Δt_b, 48 transients for each increment with a 6-s recycle delay. The evolutionary MREV8 cycle time = 12 × 3.4 μs = 40.8 μs; each $\Delta t_b/3$ evolution increment was composed of one MREV8 sequence for a total dwell time of 3 × 40.8 μs = 122.4 μs and a total evolution time of 4896 μs. The acquisition MREV8 cycle time = Δt_a = 12 × 3.4 μs = 40.8 μs, and 272 acquisition points were collected. Pulses: 45° = 0.80 μs; 90° = 1.36 μs; 135° = 1.87 μs. In all cases, the chemical shift scale is corrected for MREV8 scaling of 0.499.

The position of the isotropic peak in the evolution dimension was measured with respect to the transmitter position, and the data are plotted in Fig. 5a. The slope of the linear fit gives the scaling factor as 0.499 $\pm$ 0.002. The values for the FWHH of the isotropic peak were invariant to the transmitter offset.

The effective evolution spectral width, already reduced by a factor of 2 by the MREV8 scaling factor, is reduced by a further factor of 3 by the MAT component of the experiment according to Eq. 1. This restricted spectral width in the evolution dimension, in principle, limits the extent to which CSA patterns of vastly different resonance frequencies can be separated. Of the three naturally abundant spin-$\frac{1}{2}$ nuclei, the ^{19}F nucleus, with its large chemical shift interaction, is most sensitive to this limitation. Nevertheless, with evolutionary MREV8 cycles times as short as 24 μs, an effective evolutionary spectral width of 41.7 kHz is achievable which, at a field strength of 4.7 T, means a chemical shift range of ~75 ppm after accounting for the MREV8 scaling factor.

The ^{19}F MP-MAT NMR spectrum of a mixture of AgTFA and calcium difluoride. A physical mixture of AgTFA (0.442 g, 3.82 mmol) and CaF_2 (0.234 g, 3.00 mmol, $\delta_{iso} = -106$ ppm) was prepared to give a model two-site system to demonstrate

that the MP-MAT technique is applicable to multiple-site cases. The isotropic chemical shifts of the two components differ by 35 ppm (*41*). Since there is no anisotropy in the CaF_2 chemical shift, the MP-MAT spectrum should indicate whether there is any intensity contamination between different isotropic signals.

Figure 6 shows the ^{19}F MP-MAT NMR contour plot of the AgTFA/calcium difluoride mixture with sum projections in both dimensions. Two peaks in the F_1 isotropic evolution dimension are clearly resolved, with FWHH values of 680 (AgTFA) and 530 (CaF_2) Hz. The transmitter has been placed between the two peaks at 188.294273 MHz. The absence of ghost or pedestal artifacts in both dimensions, often seen with multiple-pulse sequences, demonstrates that the addition of magnetization developed under MREV8 conditions is consistent with the MAT requirements.

(d) Resolution Enhancement of the Isotropic Dimension

For the separation of CSA powder patterns of very similar isotropic chemical shifts, the resolution in the F_1 evolution dimension is crucial. The value for the AgTFA linewidth of the F_1 sum projection in the ^{19}F MP-MAT experiment depicted in Fig. 4 is 450 Hz. This FWHH is much larger than similar measurements with AgTFA under 1-dimensional MAS conditions (FWHH = 21 Hz at ν_{rot} = 2249 Hz). Attempts to narrow the linewidth of a stationary sample of powdered CaF_2 by adjustments of the magnet shims were unsuccessful. However, when the CaF_2 ^{19}F spectrum was collected under MAS conditions, the linewidth dropped considerably in value. The above observations indicate that the broadening of the ^{19}F peak arises from the inhomogeneity of the magnetic field at the sample due to bulk magnetic susceptibility effects. We now report several strategies to reduce the linewidth in the evolution dimension and thus increase the resolution of the 2-D MP-MAT experiment.

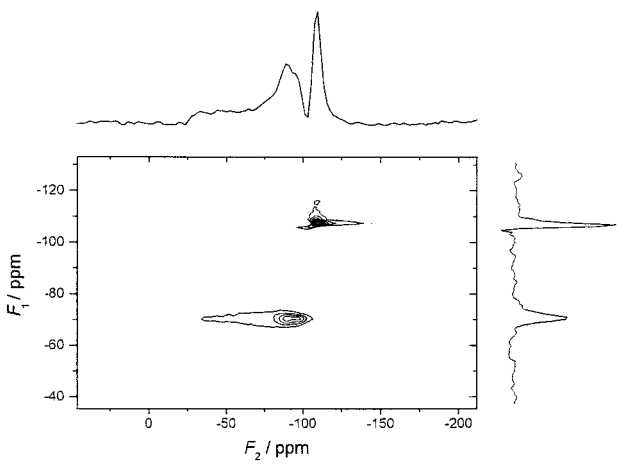

FIG. 6. ^{19}F MP-MAT NMR spectrum (188.2976 MHz) of AgTFA/calcium difluoride mixture collected at a rotor spinning speed of 71.5 Hz (τ_{rot} = 13.986 ms). Fifty $\Delta t_b/3$ increments of a 36.0-μs MREV8 cycle were collected (total dwell time = 108.0 μs) for a total evolution time of 5400 μs. Each t_a acquisition was collected 16 times using a 40.8 μs MREV8 cycle with 256 points and using a recycle delay of 6 s; the total experimental time was 2.7 h. The floor and ceiling were set to 5 and 85% I_{max}, respectively, with contour increments of 10% I_{max}. The F_1 and F_2 spectra are the sum projections. The chemical shift scale is corrected for MREV8 scaling using a value of 0.499.

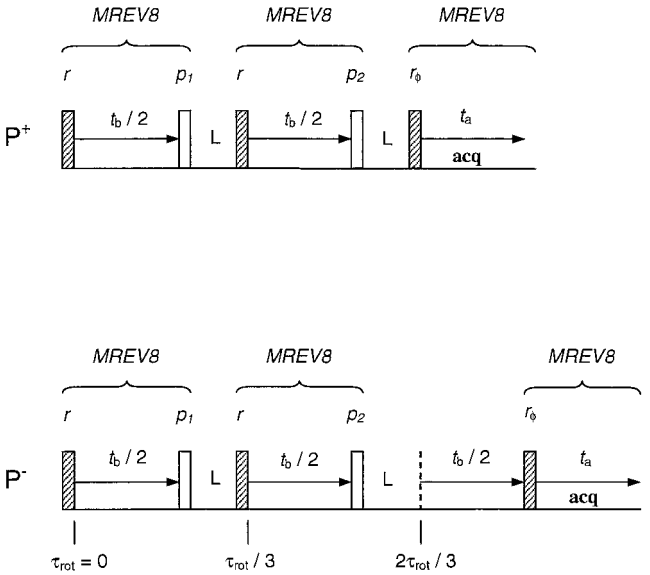

FIG. 7. The MP-MAT$^{\pm}$ pulse sequence resulting from the incorporation of MREV8 multiple pulse homonuclear decoupling into the MAT$^{\pm}$ sequence of Gan and Ernst (*6*). Note that the "plus" and "minus" variants differ in the acquisition of the t_a FID as well as in the phases of the receiver and pulses p_x. The phase table is given in Table 3. MREV8 multiple-pulse decoupling in the two dimensions are as in Figs. 1b and 1c.

Sample spinning. ^{19}F MP-MAT NMR experiments were carried out using AgTFA at sample spinning speeds between ν_{rot} = 45 and 408 Hz. The values of the FWHH for the summed F_1 projections as a function of the frequency of sample magic-angle rotation are reported in Fig. 5b as open circles. The linewidths drop considerably to 210 Hz at ν_{rot} = 408 Hz. Due to the restriction of the total evolution time to one rotor period, faster spinning speeds will lead to truncation of the evolution signal. Furthermore, at MAS speeds greater than the ^{19}F natural linewidth, a spinning-sideband manifold rather than a pseudo-static CSA pattern is collected.

The MP-MAT$^{\pm}$ pulse sequence. Additional resolution enhancement is achieved by modification of the MP-MAT pulse sequence according to the MAT$^{\pm}$ pulse sequence of Gan and Ernst (*6*). Rather than collecting three t_b evolutionary increments, two are collected, and the sequence generates a sheared spectrum. A shearing transformation is easily applied in subsequent data processing to give a spectrum with the CSA patterns parallel to the acquisition dimension. Furthermore, if the t_a and t_b increments are synchronized to an integral multiple of the rotor period, rotational echoes in the acquisition dimension can be used to extend the time-domain signal of the evolution dimension. The consequence of this data shifting is enhanced digital resolution in the evolution dimension. The

TABLE 3
The Basic Phase Table for the MP-MAT$^{\pm}$ Pulse Sequence in Fig. 7

	F_1				F_2				F_3				F_4			
nt	1	2	3	4	5	6	7	8	9	10	11	12	13	14	15	16
r	*Y*	*Y*	*Y*	*Y*	*Y*	*Y*	*Y*	*Y*	*Y*	*Y*	*Y*	*Y*	*Y*	*Y*	*Y*	*Y*
p_1	$\bar{Y}$	$\bar{Y}$	$\bar{Y}$	$\bar{Y}$	*X*	*X*	*X*	*X*	$\bar{Y}$	$\bar{Y}$	$\bar{Y}$	$\bar{Y}$	*X*	*X*	*X*	*X*
p_2	$\bar{Y}$	$\bar{Y}$	$\bar{Y}$	$\bar{Y}$	*X*	*X*	*X*	*X*	*X*	*X*	*X*	*X*	$\bar{Y}$	$\bar{Y}$	$\bar{Y}$	$\bar{Y}$
r_ϕ	135	45	90	90	135	45	90	90	135	45	90	90	135	45	90	90
	Y	$\bar{Y}$	*X*	$\bar{X}$	*Y*	$\bar{Y}$	*X*	$\bar{X}$	*Y*	$\bar{Y}$	*X*	$\bar{X}$	*Y*	$\bar{Y}$	*X*	$\bar{X}$
rcvr	*Y*	$\bar{Y}$	*X*	$\bar{X}$	*Y*	$\bar{Y}$	*X*	$\bar{X}$	*Y*	$\bar{Y}$	*X*	$\bar{X}$	*Y*	$\bar{Y}$	*X*	$\bar{X}$
Sum	*X*				$\bar{X}$				$\bar{Y}$				$\bar{Y}$			

	F_5				F_6				F_7				F_8			
nt	1	2	3	4	5	6	7	8	9	10	11	12	13	14	15	16
Sum	*X*				$\bar{X}$				*Y*				*Y*			

Note. The P^+ (top) and P^- (bottom) data sets are collected with variation of the required phase for the sum $P^+ = \sum_{i=1}^{4} F_i$ and $P^- = \sum_{i=5}^{8} F_i$; *nt* represents the transition number.

MP-MAT$^{\pm}$ sequence is depicted in Fig. 7 and the pulse phases are recorded in Table 3. Each of the eight different FIDs were collected independently using the same receiver phase and combined to give the real and imaginary FIDs as described above.

The improvement in the AgTFA linewidths at $\nu_{rot} = 408$ Hz is dramatic, as indicated by the noncircle symbols in Fig. 5b. The MP-MAT$^{\pm}$ sequence gives an immediate improvement relative to the MP-MAT sequence at $\nu_{rot} = 408$ Hz which may arise from the development of the evolution signal over two rather than three evolutionary periods. As the length of the evolution signal is extended from 4896 to 19584 μs by rotational echo data shifting, the linewidth drops to 50 Hz.

Resolution enhancement using the rotational echo t_b extension technique also increases the noise in the ^{19}F MP-MAT$^{\pm}$ as indicated in the sum F_1 projections in Fig. 8. Ridge features, reminiscent of spinning sidebands, lie parallel to the F_2 axis and increase in prominence as the number of rotational echo extensions of the evolutionary signal increase. These features have been described by Grant and co-workers for the 5-π MAT and FIREMAT sequences which employ evolutionary block replication techniques (*11, 12*). In the present case, ridge features arising from the difference in the decay of magnetization intensity along the t_a acquisition and t_b evolution dimensions are understood in terms of a sinex/x effect resulting from truncation of the evolution time signal in discrete blocks. In the acquisition dimension, magnetization decays as $\exp(-t_a/T_2)$, and as $\exp(-t_b/T_2)$ in the evolution dimension, T_2 being the transverse magnetization relaxation time constant. The extended evolution signal is created by taking the first rotational echo, which has an intensity of $I_a = I_0\exp(-\tau/T_2)$, and adding it to the evolution dimension terminus at time $2\tau/3$, which has an intensity $I_b = I_0\exp(-(2\tau/3)/T_2)$. Clearly, $I_b > I_a$; similar intensity differences occur at each rotational echo extension at times $2k\tau/3$, where $k =$ the number of rotational echoes. The resulting extended t_b evolutionary signal is characterized by a stepped decay function which, in turn, leads to the observed sinex/x artifacts.

In theory, the decay of magnetization intensity in the evolution dimension will step down as a function of k rotational echo extensions. Furthermore, the noise of the evolution signal in each block may add coherently as a function of k. This feature becomes more pronounced when T_2 is of the order of or less than the rotor period τ_{rot}. In practice, however, errors in rotor synchronization and MREV8 pulse imperfections contribute to additional loss of signal magnetization and cause the intensity of the extended evolution signal to step up as a function of k. Both truncation and noise-coherence effects can be treated in part by application of an exponential damping function to the acquisition domain before rotational echo extension of the t_b signal. While this treatment reduces the prominence of the artifact signals, it also decreases the digital resolution and hence increases the linewidth of the resulting signals (Fig. 8d).

Evolution MREV8 cycle time t_c. In 1-dimensional multiple-pulse NMR experiments, the cycle time t_c is determined by the 90° pulse duration and the τ delay between pulses. To achieve a large spectral width, t_c should be as short as possible. Since the signal must be sampled at least once during the cycle, the probe ring-down and dead-time characteristics determine the minimum multiple-pulse τ value and hence t_c. Short t_c values are also desirable to improve the effectiveness of the homonuclear dipolar averaging.

Indirect sampling of the evolutionary signal allows multiple-pulse cycle times to be shorter than in the directly sampled acquisition dimension. In addition to increasing the spectral width, use of a τ delay of 2.0 μs ($t_c = 24.0$ μs) reduces slightly

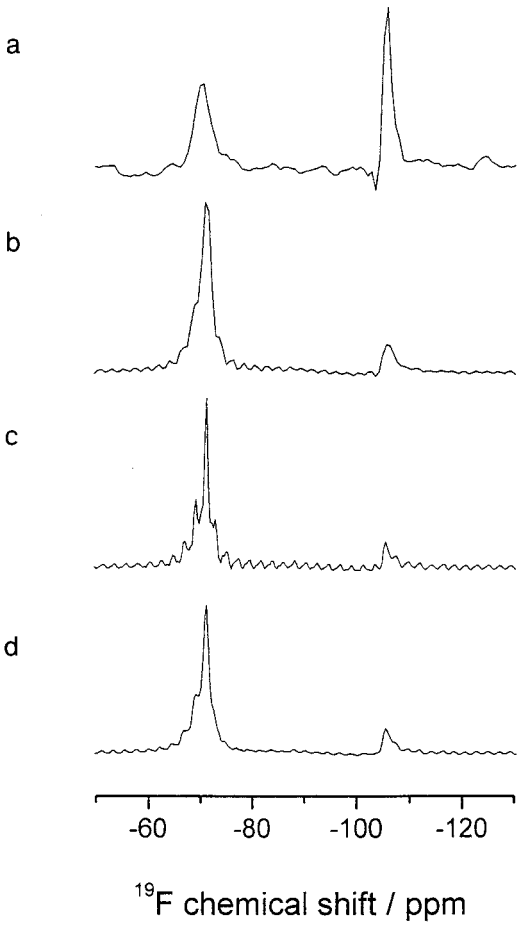

FIG. 8. Resolution enhancement in the sum isotropic chemical shift projections of the ^{19}F 2-D isotropic chemical shift versus CSA spectrum of AgTFA. (a) MP-MAT, ν_{rot} = 71.5 Hz, (b) MP-MAT$^{\pm}$, ν_{rot} = 408 Hz with no rotational echo extensions in t_b, (c) MP-MAT$^{\pm}$, ν_{rot} = 408 Hz with two rotational echo extensions in t_b, (d) MP-MAT$^{\pm}$, ν_{rot} = 408 Hz with 200 Hz exponential linebroadening applied to the acquisition dimension prior to two rotational echo extensions in t_b.

the linewidth in the t_b dimension of AgTFA at ν_{rot} = 45 Hz to 330 Hz compared to 350 Hz using a τ delay of 3.0 μs (t_c = 36.0 μs). It should be feasible to incorporate more sophisticated multiple-pulse decoupling schemes such as BR24 (*42*) and CORY24 (*36*) as well as windowless and semi-windowless variants. It is anticipated that these modifications will contribute to an improvement in resolution.

Final comments on resolution enhancement. Three approaches to improve the resolution of the MP-MAT experiment have been investigated: (a) increased sample rotation, (b) improvements in the MAT component of the experiment, and (c) shorter multiple-pulse t_c cycle times. Each strategy has led to resolution enhancement as detailed above. It is noted, however, that these three investigations by no means exhaust the list of potential improvements to the technique. Grant and co-workers have shown the benefit of a rotor synchronization strategy by which the MAT pulses are triggered by optical sensing of the sample rotor position (*5*). We note that the sample rotation conditions described herein ($\pm$0.5 Hz) give an error in rotor period timing of $\pm$100 μs at a spinning speed of ν_{rot} = 71.5 Hz. The error is comparable to the evolutionary dwell time and is likely to give rise to error in the isotropic chemical shift dimension; this error is manifested in (a) a low signal-to-noise ratio and (b) additional magnetization decay resulting in poorly resolved signals.

The present MAT experiments fall into the "projection" class of MAT experiments (*11*). Isotropic chemical shift and CSA correlation spectra are also obtained from the "5-π" class of MAT experiments. The recent FIREMAT version of a 5-π MAT experiment for dilute spin-$\frac{1}{2}$ nuclei offers a significant improvement in the signal-to-noise ratio (*11*). Analogous 5-π MAT experiments incorporating multiple-pulse decoupling sequences will, in principle, offer similar advantages to abundant spin-$\frac{1}{2}$ nuclei. A 5-π MP-MAT sequence is more appropriate for nuclei with large CSA values such as ^{19}F and ^{31}P than for ^{1}H, which is better suited to the projection MAT experiment because of the small ^{1}H CSA values.

More efficient homonuclear dipolar decoupling gives narrower linewidths in the t_b isotropic dimension. This improvement may be achieved by decreasing the multiple-pulse cycle time and by employing multiple-pulse dipolar decoupling schemes which average to zero the higher order homonuclear dipolar interaction terms. Such sequences include the BR24 and CORY24 sequences as well as the windowless and semi-windowless versions. One must select compensation pulse durations and phases appropriate to the effective magnetization precession axis.

CONCLUSIONS

We have demonstrated the use of the MAT experiment on abundant spin-$\frac{1}{2}$ nuclei where the homonuclear dipolar interaction is dominant. This interaction is suppressed though the incorporation of an MREV8 homonuclear dipolar decoupling sequence into the MAT experiment. The quadrature nature of the MAT experiment is preserved, thereby maximizing the spectral width of the experiment and the effectiveness of the MREV8 sequence in suppressing the homonuclear dipolar interaction.

ACKNOWLEDGMENTS

The authors thank Dr. H. Cho (PNNL, Richmond, WA) and Mr. Barry J. Say for helpful discussions. We are grateful to Dr. G. McGeorge and Prof. D. M. Grant for information on the FIREMAT experiment prior to publication. EBB thanks the Natural Sciences and Engineering Research Council of Canada for a postdoctoral fellowship 1996–1998. The work was supported by EPSRC Grant GR/L02906.

REFERENCES

1. J. Z. Hu, W. Wang, and R. J. Pugmire, Magic angle turning and hopping, *in* "Encyclopedia of NMR" (R. K. Harris and D. M. Grant, Eds.), pp. 2914–2921, Wiley, Chichester (1996).

2. K. Schmidt-Rohr and H. W. Spiess, "Multidimensional Solid-State NMR and Polymers," pp. 188–195, Academic Press, London (1994).
3. A. Bax, N. M. Szeverenyi, and G. E. Maciel, Correlation of isotropic shifts and chemical shift anisotropies by two-dimensional Fourier-transform magic-angle hopping NMR spectroscopy, *J. Magn. Reson.* **52,** 147–152 (1983).
4. Z. Gan, High-resolution chemical shift and chemical shift anisotropy correlation in solids using slow magic angle spinning, *J. Am. Chem. Soc.* **114,** 8307–8309 (1992).
5. J. Z. Hu, W. Wang, F. Liu, M. S. Sollum, D. W. Alderman, R. J. Pugmire, and D. M. Grant, Magic-angle-turning experiments for measuring chemical-shift-tensor principal values in powdered solids, *J. Magn. Reson. A* **113,** 210–222 (1995).
6. Z. Gan and R. R. Ernst, An improved 2D magic-angle-turning pulse sequence for the measurement of chemical-shift anisotropy, *J. Magn. Reson. A* **123,** 140–143 (1996).
7. J. C. Facelli, A. M. Orendt, Y. J. Jiang, R. J. Pugmire, and D. M. Grant, Carbon-13 chemical shift tensors and molecular conformation of anisole, *J. Phys. Chem.* **100,** 8268–8272 (1996).
8. G. Zheng, J. Z. Hu, X. D. Zhang, L. Shen, C. Ye, and G. A. Webb, Quantum chemical calculation and experimental measurement of the ^{13}C chemical shift tensors of vanillin and 3,4-dimethoxybenzaldehyde, *Chem. Phys. Lett.* **266,** 533–536 (1997).
9. M. Strohmeier, A. M. Orendt, J. C. Facelli, M. S. Solum, R. J. Pugmire, R. W. Parry, and D. M. Grant, Solid state N-15 and C-13 NMR study of several metal 5,10,15,20-tetraphenylporphyrin complexes, *J. Am. Chem. Soc.* **119,** 7114–7120 (1997).
10. G. McGeorge, J. Z. Hu, C. L. Mayne, D. W. Alderman, R. J. Pugmire, and D. M. Grant, Technique for importing greater evolution resolution in multidimensional NMR spectrum, *J. Magn. Reson.* **129,** 134–144 (1997).
11. J. K. Harper, G. McGeorge, and D. M. Grant, Solid-state C-13 chemical shift tensors in terpenes—Part I. Spectroscopic methods and chemical shift structure correlations in caryophyllene oxide, *Magn. Reson. Chem.* **36,** S135–S144 (1998).
12. D. W. Alderman, G. McGeorge, J. Z. Hu, R. J. Pugmire, and D. M. Grant, A sensitive, high-resolution magic-angle-turning experiment for measuring chemical-shift-tensor principal values, *Mol. Phys.* **95,** 1113–1126 (1998).
13. "Solid-state NMR of Polymers" (I. Ando and T. Asakura, Eds.), Elsevier, Amsterdam (1998).
14. G. Engelhardt and H. Koller, ^{29}Si NMR of inorganic solids, *NMR Basic Prin. Prog.* **31,** 1–29 (1994).
15. C. T. Kresge, M. E. Leonowicz, W. J. Roth, J. C. Vartuli, and J. S. Beck, Ordered mesoporous molecular sieves synthesized by a liquid–crystal template mechanism, *Nature* **359,** 710–712 (1992).
16. G. Govil and R. V. Hosur, Conformation of biological molecules: New results from NMR, *NMR Basic Prin. Prog.* **20,** 1–216 (1982).
17. U. Haeberlen, Achievements of multiple-pulse NMR, *Phil. Trans. R. Soc. Lond. A* **299,** 497–504 (1981).
18. R. K. Harris, P. Jackson, L. H. Merwin, B. J. Say, and G. Hagele, Perspectives in high-resolution solid-state NMR, with emphasis on combined rotation and multiple-pulse spectroscopy, *J. Chem. Soc. Faraday Trans 1* **84,** 3649–3672 (1988).
19. E. B. Brouwer and R. K. Harris, Setting the magic angle for ^{19}F MAS NMR using *p*-tert-butylcalix[4]arene-α,α,α-trifluorotoluene, submitted for publication.
20. D. P. Burum, M. Linder, and R. R. Ernst, A new tune-up NMR pulse cycle of minimizing and characterizing pulse transients, *J. Magn. Reson.* **43,** 463–471 (1981).
21. T. M. Barbara and L. Baltusis, Phase-cycled, multiple-window-acquisition, multiple-pulse NMR spectroscopy, *J. Magn. Reson. A* **106,** 182–187 (1994).
22. S. A. Smith, T. O. Levante, B. H. Meier, and R. R. Ernst, Computer simulations in magnetic resonance. An object-oriented programming approach, *J. Magn. Reson. A* **106,** 75–105 (1994). GAMMA Version 3.5β by S. A. Smith and T. O. Levante; National High Magnetic Field Laboratory, 1800 E. Paul Dirac Drive, Tallahassee, FL 32306-4005; ssmith@magnet.fsu.edu; http://gamma.magnet.fsu.edu.
23. J. H. Shirley, Solution of the Schrödinger equation with a Hamiltonian periodic in time, *Phys. Rev. B* **138,** 979–987 (1965).
24. A. Schmidt and S. Vega, The Floquet theory of NMR spectroscopy of single spins and dipolar coupled spin pairs in rotating solids, *J. Chem. Phys.* **96,** 2655–2680 (1992).
25. U. Haeberlen, High resolution NMR in solids: Selective averaging, *in* "Advances in Magnetic Resonance, Supplement 1," Academic Press, London (1976).
26. M. M. Maricq and J. S. Waugh, NMR in rotating solids, *J. Chem. Phys.* **70,** 3300–3316 (1979).
27. U. Haeberlen and J. S. Waugh, Coherent averaging effects in magnetic resonance, *Phys. Rev.* **175,** 453–467 (1968).
28. H. W. Spiess, Rotation of molecules and nuclear spin relaxation, *in* "NMR Basic Principles and Progress, Volume 15: Dynamic NMR Spectroscopy" (P. Diehl, E. Fluck, and R. Kosfeld, Eds.), pp. 55–214, Springer-Verlag, New York (1978).
29. J. M. Hammersley and D. C. Handscomb, D. C. Monte Carlo methods, *in* "Meuthen's Monographs on Applied Probability and Statistics" (M. S. Bartlett, Ed.), Wiley, New York (1964).
30. H. Wozniakowski, Average case complexity of multivariate integration, *Bull. Am. Math Soc.* **24,** 185–194 (1991).
31. H. Conroy, Model Schrödinger equation. VIII. A new method for the evaluation of multidimensional integrals, *J. Chem. Phys.* **47,** 5307–5318 (1967).
32. V. B. Cheng, H. H. Suzukawa, Jr., and M. Wolfsberg, Investigations of a nonrandom numerical method for multidimensional integration, *J. Chem. Phys.* **59,** 3992–3999 (1973).
33. J. S. Waugh, L. M. Huber, and U. Haeberlen, Approach to high-resolution NMR in solids, *Phys. Rev. Lett.* **20,** 180–182 (1968).
34. W.-K. Rhim, D. D. Elleman, and R. W. Vaughan, Enhanced resolution for solid-state NMR, *J. Chem. Phys.* **58,** 1772–1774 (1973).
35. P. Mansfield, Symmetrized pulse sequences in high resolution NMR in solids, *J. Phys. C* **4,** 1444–1452 (1971).
36. D. G. Cory, A new multiple-pulse cycle for homonuclear dipolar decoupling, *J. Magn. Reson.* **94,** 526–534 (1991).
37. H. Cho, Tilted-axis precession and phase-sensitive detection of nuclear magnetization, *J. Magn. Reson. A* **121,** 8–22 (1996).
38. P. Caravatti, L. Braunschweiler, and R. R. Ernst, Heteronuclear correlation spectroscopy in rotating solids, *Chem. Phys. Lett.* **100,** 305–311 (1983).
39. P. Jackson, Short-cycle-time fluorine-19 CRAMPS, *J. Magn. Reson.* **90,** 391–396 (1990).
40. M. Mehring, R. G. Griffin, and J. S. Waugh, ^{19}F shielding tensors from coherently narrowed NMR powder spectra, *J. Chem. Phys.* **55,** 746–755 (1971).
41. R. K. Harris and P. Jackson, High resolution fluorine-19 magnetic resonance of solids, *Chem. Rev.* **91,** 1427–1440 (1991).
42. D. P. Burum and W.-K. Rhim, Analysis of multiple pulse NMR in solids. III, *J. Chem. Phys.* **71,** 944–956 (1979).